Title	Temperature measurement for in-situ crack monitoring under high-frequency loading
Author(s)	Naoe Takashi, Xiong Z., Futakawa Masatoshi
Citation	Journal of Nuclear Materials,506,p.12-18
Text Version	Preprint
URL	https://jopss.jaea.go.jp/search/servlet/search?5057124
DOI	https://doi.org/10.1016/j.jnucmat.2017.12.019
Right	©2017 Elsevier B.V.

Temperature measurement for in-situ crack monitoring under high-frequency loading

Takashi Naoe[a], Xiong Zhihong[b], Masatoshi Futakawa[a]

[a]Japan Atomic Energy Agency, Tokai-mura, Naka-gun, Ibaraki 319-1195, Japan.
[b]Sino-French Institute of Nuclear Engineering and Technology of Sun Yat-sen University, Tangjiwan Zhuhai, Guangdong Province, 519082, China

Abstract

A liquid mercury target vessel, composed of type 316L stainless steel and used in a pulsed spallation neutron source, suffers not only from proton and neutron damage but also cyclic impact stresses caused by proton beam-induced pressure waves. In a previous study, we carried out an ultrasonic fatigue test to gigacycles and observed that the specimen surface temperature rose abruptly just before failure. To understand the mechanism of this temperature rise, the temperature distribution of the specimen surface was measured using a thermography instrument during an ultrasonic fatigue test. The result showed that the temperature rose locally, especially at the crack tip, and the peak position moved with crack propagation. Furthermore, nonlinear structural analysis by LS-DYNA was performed to clarify the mechanism of this temperature rise. The analytical results showed that the heat due to plastic deformation at the crack tip is the dominant factor underlying the temperature rise rather than friction between crack surfaces.

Keywords: Gigacycle fatigue, High-strain rate, Crack propagation, Temperature, Thermography, Non destructive inspection

---

Email address: `naoe.takashi@jaea.go.jp` (Takashi Naoe)

Preprint submitted to Journal of Nuclear Materials *May 18, 2018*

---

1. Introduction

A pulsed spallation neutron source, which generates neutrons by injecting high-intensity pulsed proton beams into liquid mercury, is installed at the Materials and Life science experimental Facility (MLF) in Japan Proton Accelerator Research Complex (J-PARC). A mercury enclosure vessel composed of type 316L stainless steel (316L SS), a so-called target vessel, suffers not only proton and neutron irradiation damage but also cyclic impact stress caused by proton beam-induced pressure waves [1]. The target vessel undergoes more than $2{\times}10^8$ cycles over its designed service life of 2500 MWh and/or 5 dpa (displacement per atom) which is decided temporally based on ductility under irradiation [2]. Furthermore, the strain rate at the beam window of the target vessel reaches approximately 50 1/s at the maximum. Fig. 1 shows the time responses of the stress and strain rate at the center of the beam window of the mercury target vessel at 1 MW in J-PARC, as obtained from numerical simulation. The strain rate is much higher than that of conventional fatigue loading of $\sim 10^{-1}$ 1/s.

It was reported that the fatigue strength in the gigacycle region is different from conventional fatigue strength up to millions of cycles. For example, internal nonmetallic inclusions lead to internal fracture, so-called fish-eye, at more than 10^7 cycles for high-strength steels, and it is difficult to define the fatigue limit using fatigue data for up to 10^7 cycles [3]. By contrast, in the austenitic stainless steels used as structural materials for nuclear components, fatigue data for cycle counts higher than 10^7 is insufficient [4]. It was reported that fatigue failure originating from the surface (surface fracture) is dominant in solution-annealed 316NG, whereas fish-eye fracture originating from the inclusion of pre-strained

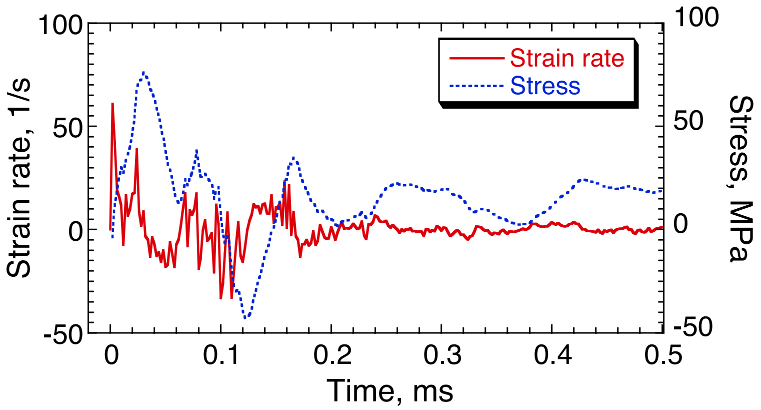

Fig. 1. Time responses of stress and strain rates of beam window for mercury target vessel at beam power of 1 MW.

material occurred in only one case [4, 5]. A remarkable reduction in the total elongation due to the nonmetallic inclusions was observed in a few 316LN specimens in a quasi-static tensile test involving post-irradiation examinations of the mercury target vessel used in the Spallation Neutron Source at Oak Ridge National Laboratory (ORNL) [6].

In previous studies, an ultrasonic fatigue test, which is one of the accelerated test methods that uses ultrasonic-resonance, was performed to investigate the gigacycle fatigue strength of 316L SS. The result showed that fatigue failure due to surface cracking occurred when the number of cycles was higher than 10^7, and obviously, the fatigue limit of up to 10^9 cycles was not reached. Furthermore, specimen temperature rose abruptly just before failure, accompanied by surface oxidation [7, 8]. Change in specimen temperature during fatigue testing has been reported in many studies. For example, Sakagami et al. developed self-reference lock-in thermography, in which a reference signal was constructed from sequential data on the thermoelastic temperature change, for remotely and non-destructively detecting the fatigue cracking [9]. Luong proposed a prediction method for detecting the fatigue limit in a low-cycle fatigue test by analyzing the temperature change due to irreversible energy dissipation obtained from infrared thermography [10]. This method was based on the detection of inflection point of the dissipated energy, which increases with stress amplitude. Akai et al. confirmed the applicability of that prediction method for the fatigue testing of 316L SS at 5 Hz from the viewpoint of change in the dissipated energy as a function of stress amplitude [11].

As for the ultrasonic fatigue test in which the strain rate is three orders of magnitude higher than that in the conventional fatigue test, Wagner et al. reported a rise in the temperature of cast aluminum-silicon alloys just before failure [12]. Krewerth et al. investigated crack initiation and crack propagation in AlSi7Mg steel by using thermography and concluded that infrared thermal measurements facilitate the exact detection of the initiation of internal, surface, and multiple cracks, as well as their propagation pass; the abrupt temperature rise due to crack propagation occured at approximately 99% of the total fatigue life of the specimen [13]. Ranc et al. developed a thermomechanical model to investigate the relationship between thermal effects and crack initiation and propagation, and concluded that the temperature field of the developed model shows a good correlation with experiment results, and crack propagation constitutes a small part of the specimen lifetime [14]. In the case of the ultrasonic fatigue test, the mechanism of temperature change during the fatigue test seems to be different from the thermoelastic effect observed in conventional fatigue, because the temperature increase is much higher than that under conventional fatigue. Specifically, during the conventional low frequency fatigue test, it is possible to observe the thermoelastic effect which oscillate with a zero-mean value with cycle because the integration time of the infrared thermography is much smaller than the cycle period. However, for the ultrasonic fatigue test, the infrared thermography integrate during many cycles and is not able to detect the thermoelastic effect.

In this fundamental study on detecting the initiation and propagation of fatigue crack by remote and non-destructive measurement, with an aim to clarify the mechanism of temperature rise just before failure, measurement of surface temperature distribution on a 316L SS specimen during an ultrasonic fatigue test was performed using infrared thermography. Furthermore, nonlinear structural analysis was performed to clarify the mechanism of temperature rise, with a focus on plastic strain, friction, and beating of the fracture surface.

2. Experiment

2.1. Materials and specimens

Type 316L stainless steel, which is the structural material of the mercury target vessel, was used for the gigacycle fatigue test. As-received materials has been heat-treated by solution-annealing (SA) at 1120°C for 7.5 min, followed by water quenching. A part of the SA plate was cold-rolled to 20% reduction in thickness for simulating irradiation-hardened material by increasing the dislocation density. This part is referred to as CW hereinafter.

Schematic drawings of the specimen designs are shown in Fig. 2. Two types of specimen were selected for the ultrasonic fatigue test an hourglass-shaped specimen and a notched plate specimen. The former was of the standard shape, the latter was selected to localize crack initiation location by notch and measure tem-

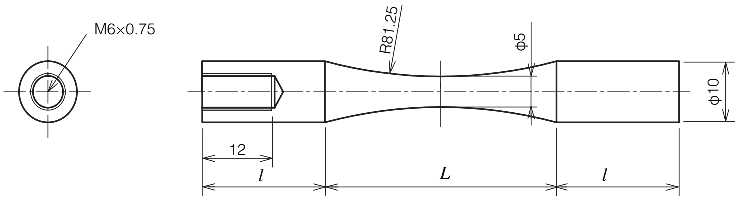

(a) Hourglass shape specimen

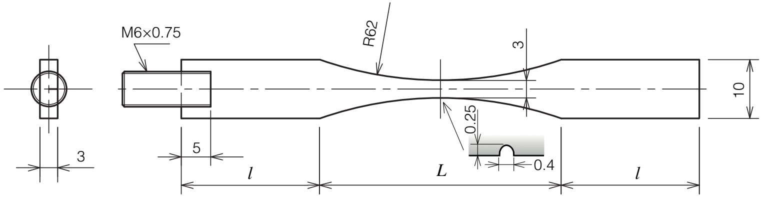

(b) Plate specimen

Fig. 2. Fatigue test specimens (Dimensions in mm)

perature distribution on a flat surface. The longitudinal direction of the specimen surface was set perpendicular to the working direction. Surface roughness of the specimens was as-machined ($Ra = 0.46$ μm) without any heat treatment. To obtain the resonance frequency of the specimen at 20 kHz, the lengths l and L of the hourglass specimen were selected according an empirical equation [4, 15] as 22.7 mm and 40 mm, respectively. For the plate specimen, given that the shape has no empirical equation,l and L were selected as 23.5 mm and 41.07 mm, respectively, based on the result of resonance analysis by FE simulation.

2.2. *Ultrasonic fatigue test*

Gigacycle fatigue tests were conducted using an ultrasonic fatigue testing system (Shimadzu, USF-2000). Fig. 3 shows a photograph of the experimental setup. Ultrasonic oscillation at the rated frequency of 20 kHz was applied to the specimen through an ultrasonic horn fixed at one end of the specimen. The stress amplitude was controlled by changing the displacement amplitude of the free-end of the specimen. The specimen was loaded in tension-compression (ratio of stress $R = \sigma_{max}/\sigma min{=}-1$). Fatigue failure in this study was defined as the point which the resonance frequency of specimen exceeded −0.5 kHz, because the resonance frequency decreases with fatigue crack initiation. Consequently, the specimen was not completely broken after the fatigue test. In addition, the fatigue test was stopped when the number of loading cycles exceeded 10^9 cycles, and the specimen was treated as an un-failed one.

To prevent temperature rise of the specimen due to internal heat arising from high-speed deformation, intermittent loading was applied during the test in addition to air cooling of the specimen surface. The loading and arresting time were selected as 0.11 s and 5 s, respectively. The cycle count in this experiment was calculated from the oscillation time under constant displacement amplitude and the resonance frequency of the specimen. It is noted that the rising and damping time of ultrasonic oscillation, in which accumulated time is approximately 6.7% of total oscillation time, were ignored. A detailed description of the ultrasonic fatigue test can be found in the literature [7].

2.3. Temperature measurement

The specimen surface temperature was continuously monitored during the fatigue test using an infrared thermometer (Keyence, IT2-02), whose spot diameter, sampling frequency, and measurement range were 1.2 mm, 5 Hz, and 0–500 °C, respectively. Furthermore, an infrared thermography device (Optris, PI160) was used to measure the temperature distribution on the specimen surface. The resolution and frame rate of the thermography device were 160×120 pixels and 100 Hz,

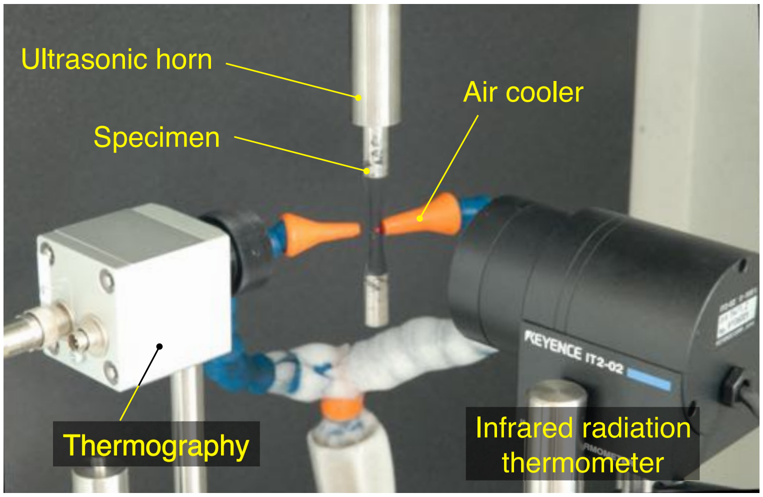

Fig. 3. Photograph of experimental setup for ultrasonic fatigue test

respectively. The temperature ranges were 0–250 °C and 150–900 °C. To stably measure temperature distribution, a black body paint with emissivity of 0.94 was sprayed on specimen surface. After the fatigue test, the specimen surface was polished slightly using an emery paper to remove the black body paint. The specimen surface was observed using a digital microscope (Keyence, VHX-900) to locate the fatigue cracks.

3. Experimental results

3.1. Fatigue strength and temperature

The relationship between stress amplitude and number of cycles to failure (S–N curve) for the SA and the CW 316L hourglass specimens are shown in Fig. 4. It can be seen that the low-cycle region for SA has a large scatter. The fatigue strength of CW is clearly higher than that of SA because of work hardening due

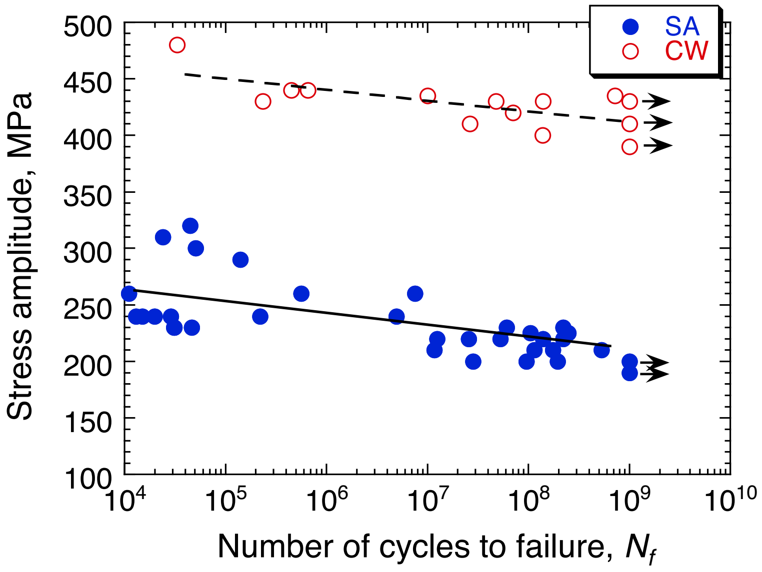

Fig. 4. S–N curves of SA and CW 316L specimens in ultrasonic fatigue test at room temperature.

to cold working. The fatigue limit up to 10^9 cycles for both SA and CW dose not seem to have been reached.

A typical example of the time response of the specimen surface temperature obtained by infrared radiation thermometer is shown in Fig. 5. The specimen and the stress amplitude are hourglass SA and 220 MPa, respectively. Given that austenitic stainless steel has low heat conductivity and large internal friction, the surface temperature of the specimen increased rapidly owing to self-heating caused by ultrasonic oscillation. The specimen temperature fluctuated within the range of 6–16 °C owing to the intermittent loading. Furthermore, in the previous study, it was confirmed that occurrence of specimen surface temperature rise about 0.35 s delayed with the ultrasonic oscillation [8].

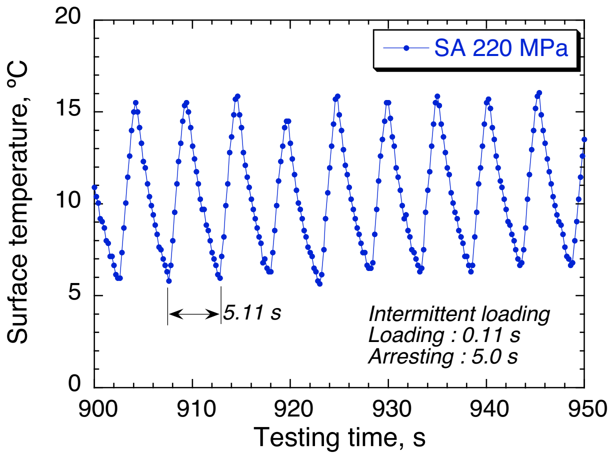

Fig. 5. Time history of specimen surface temperature for hourglass SA specimen at 220 MPa.

The rise in temperature of each intermittent loading cycle tested at 220 MPa, as shown in Fig. 5, is extracted and shown in Fig. 6, along with the results of the tests conducted at 240 MPa and 260 MPa. Note that the number of cycles was estimated based on the testing time and the effective testing frequency of ca. 430.5 Hz. In the case of testing at 220 MPa, the rise in surface temperature was maintained at around 10 °C at the maximum before failure (Region I). This temperature stabilization is caused by the balance between deformation energy (heat by ultrasonic oscillation) and heat conduction and convection (removal of heat by air cooling). In Region II, an abrupt temperature rise occurs just before failure. By contrast, for stress amplitudes of 240 MPa and 260 MPa, fatigue failure occurred in a relatively low-cycle region compared to that when the stress amplitude was 220 MPa. Temperature stabilization in these cases is not recognized because the heat due to deformation energy is higher than the heat removed by air cooling. The abrupt rise

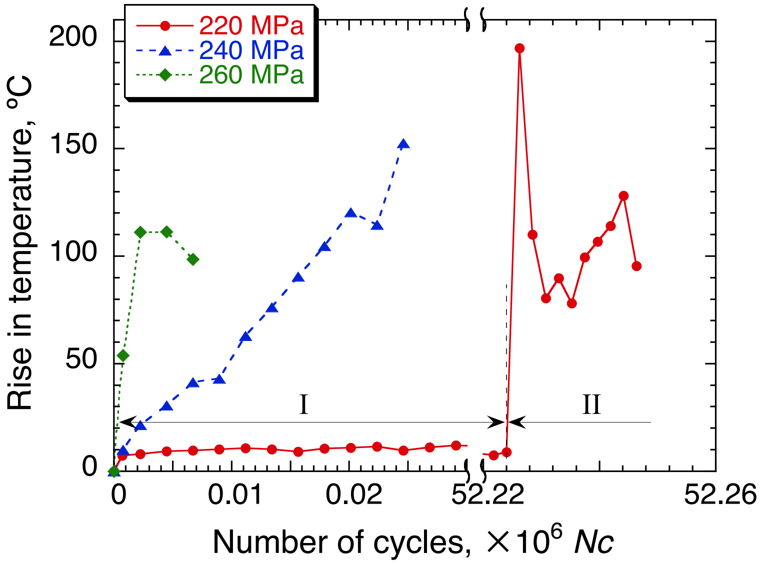

Fig. 6. Change in specimen surface temperature rise as a function of number of cycles for hourglass SA specimens. Number of cycles to failure tested at 220 MPa, 240 MPa, and 260 MPa are 5.27×10^7, 2.86×10^4, and 8.81×10^3, respectively.

in temperature just before failure is hardly recognized owing to a continuous rise in temperature during the test. It is noted that the rated displacement amplitude at the end of specimen for stress amplitudes of 220 MPa, 240 MPa, and 260 MPa are 16.8 µm, 18.4 µm, and 19.9 µm, respectively.

3.2. Temperature distribution

3.2.1. Hourglass specimen

Fig. 7 shows the specimen surface temperature distributions just before failure of the hourglass CW specimen tested at 420 MPa, as obtained from the thermography. Additionally, the changes in the peak temperature of specimen surface in the fields of each thermography image as a function of the number of cycles are shown in Fig. 8. An abrupt temperature rise just before failure is recognized. It can be seen from Fig. 7 that the surface temperature around the center part of specimen is almost homogeneous for 2.12117×10^8 (N_1) cycles. For N_1+2000 cycles, a localized temperature rise is recognized on the right-side of the specimen, as shown in Fig. 7(b). Then, the peak temperature rises and the high-temperature area increases in size with an increase in the number of cycles (Figs. 7(c), (d)); in particular, high-temperature regions can be seen recognized on both sides of Fig. 7(d). Fig. 9 shows a photograph of the specimen surface after the fatigue test. This photograph was generated as a combined confocal image by using the laser microscope and rotating the circular specimen surface. It can be seen that the multiple cracks are recognized on both sides of photograph (Area 1 and 2), and the area is coincident with the area of temperature rise recognized in Fig. 7(d). Therefore, the localized temperature rise is thought to be related to fatigue crack initiation and/or propagation.

To observe the fatigue crack initiation and propagation more precisely, a notched plate specimen approximately 0.25 mm in depth was used for temperature measurement because such a specimen can limit crack initiation location. Fig. 10 shows the surface temperature distributions of the notched SA plate specimen. Here the stress amplitude and the number of cycles to failure are 190 MPa and 2.97×10^5 cycles. It is noted that the stress amplitude was estimated while ignoring notch shape. The temperature ranges in thermography before test and during the test were selected as 0–250 °C and 150–900 °C, respectively. Points A (x = 0 mm) and B (x = 3 mm) represent both sides of the specimen in the center part. It can be seen that the maximum temperature increases gradually with an increase in the number of cycles, and the position of the maximum temperature moves from

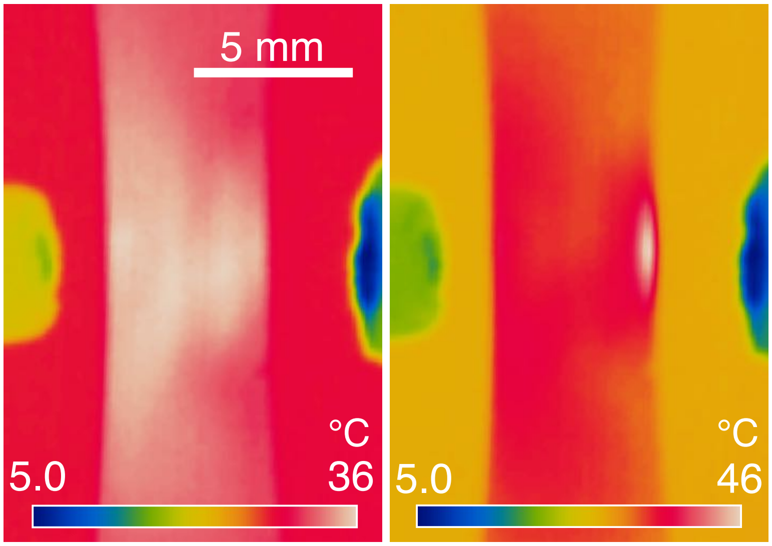

(a) $N_1 = 2.12117 \times 10^8$ cycles (b) $N_2 = N_1 + 2000$ cycles

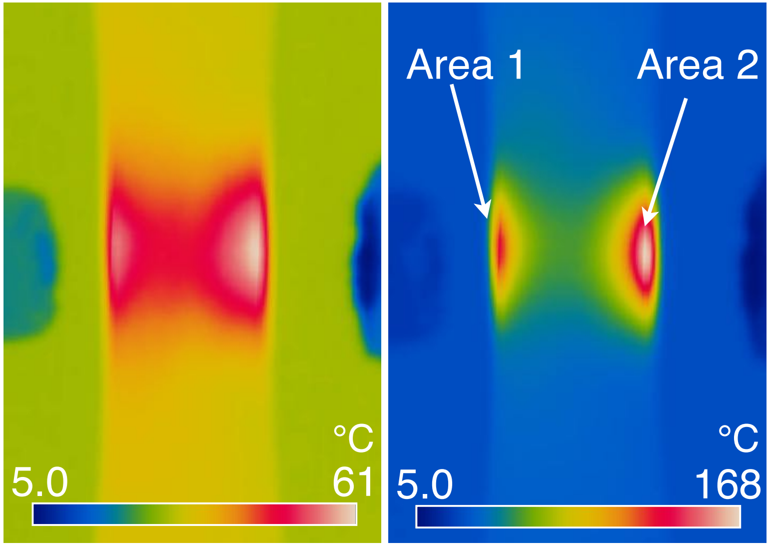

(c) $N_3 = N_1 + 6000$ cycles (d) $N_4 = N_1 + 12000$ cycles

Fig. 7. Temperature distributions of specimen surface obtained from thermography. Hourglass CW specimen tested at 420 MPa and failed at 2.121×10^8 cycles.

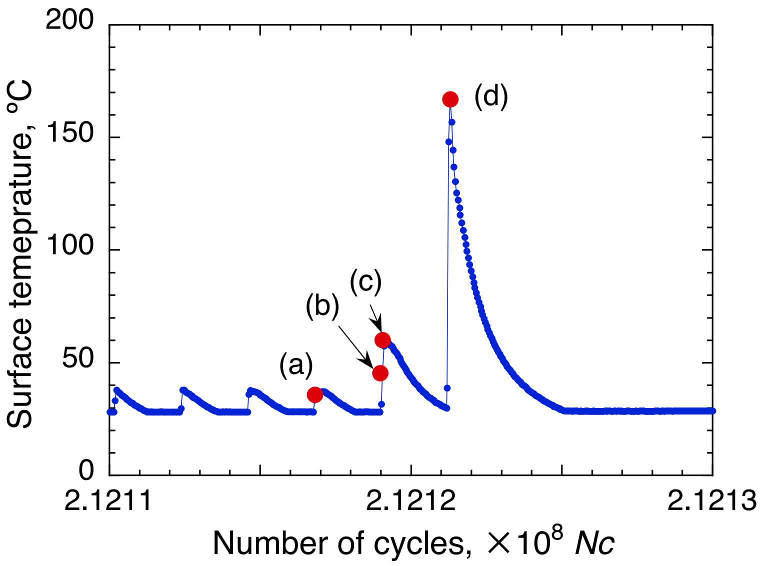

Fig. 8. Change in peak temperature of specimen surface as a function of number of cycles for hourglass CW specimen tested at 420 MPa. (a)–(d) marked in the figure correspond to the number of cycles in Fig. 7.

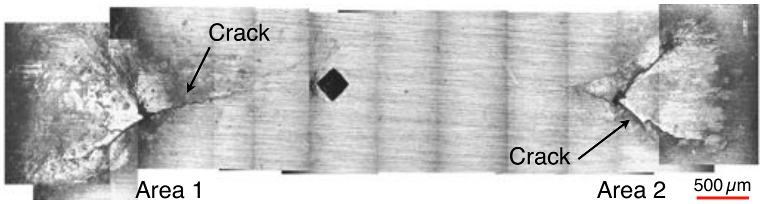

Fig. 9. Fatigue crack on 20% CW 316L specimen surface (tested at 420 MPa, failed at $2.13{\times}10^8$ cycles)

notched side A to the other side B.

Fig. 11 shows the sequence of the maximum temperature position for each loading cycle overlaid on a macroscopic image of the specimen surface after the fatigue test. Here, (b)–(f) marked in the figure denote the number of cycles, as shown in Fig. 10. The position of the maximum temperature moves with an increase of the number of cycles, although the positions of markers (e) and (f) remained the same owing to lack of resolution (approximately 0.09 mm/pixel). Furthermore, the maximum temperature was recorded almost on the trajectory of the fatigue crack. Thus, the abrupt temperature rise just before fatigue failure is attributed to crack propagation, and the position of the maximum temperature is seemingly at the tip of the crack.

4. Numerical simulation

4.1. Model for simulation

The possible mechanisms of temperature rise during the ultrasonic fatigue test just before failure are plastic strain around crack and friction heating by beating and/or sliding on the fracture surface. To clarify the dominant factor underlying the temperature rise, a finite element (FE) simulation was performed using a non-linear structural analysis software application called LS-DYNA [16].

Fig. 12 shows the FE model used for the simulation. The dimensions of the model are the same as that of the hourglass specimen shown in Fig. 2(a). Hexahedral elements measuring at least 0.2×0.1×0.1 mm, were employed in the model. The total number of nodes and elements were approximately 276000 and 259000, respectively. One end of model was oscillated with an amplitude of 20 µm at a frequency of 20 kHz. Isotropic thermal heat transfer was considered with thermal

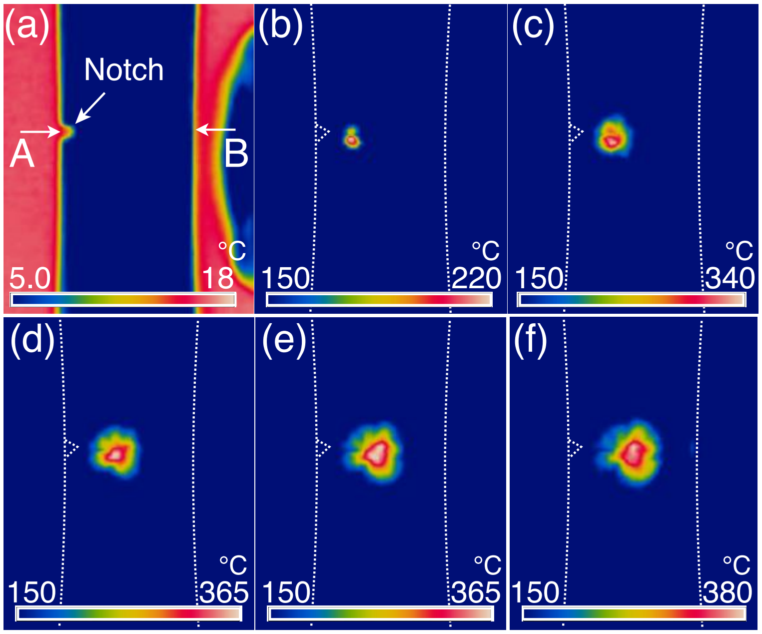

Fig. 10. Surface temperature distributions of SA plate specimen (a) before fatigue test, (b) $N_1 = 259064$ cycles, (c) N_1+400 cycles, (d) N_1+800 cycles, (e) N_1+1200 cycles, and (f) $N_1 + 1600$ cycles.

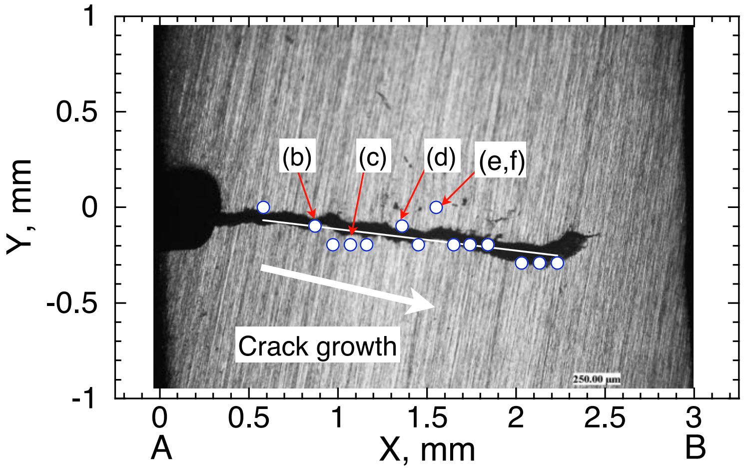

Fig. 11. Movement profile of maximum temperature position and image of fatigue crack of notched SA316L plate specimen tested at 190 MPa and failed at 2.97×10^5 cycles.

conductivity and thermal expansion coefficient of 16.0 W/m·°C and 17.3×10^{-6}/°C, respectively. The specimen surface was subjected to an adiabatic boundary condition. The initial temperature of the specimen was set to 20 °C. The kinematic hardening rule was applied to the material model to consider the Bauschinger effect. Young's modulus, yield stress, hardening coefficient, and hardening parameter were 193 GPa, 205 MPa, 1930 MPa, and 0.5, respectively. To investigate the effect of crack length on the temperature rise, the ratio of crack length to diameter, a/D, was changed parametrically from 0.09 to 0.45. The gap between the crack interfaces (fracture surface) were set constant to 2 μm, and the static and dynamic coefficients of friction were set to 0.4 for calculating the friction energy. The locations at the tip of the crack on the fracture surface and at the tip of the crack on the specimen surface are called the crack tip and crack edge, respectively.

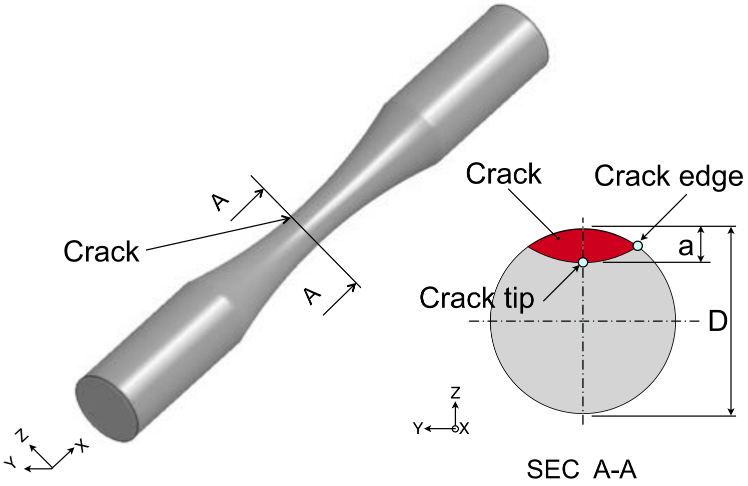

Fig. 12. FEM model for simulation. Specimen dimensions are the same as those of the hourglass specimen shown in Fig. 2(a).

The estimable factors for temperature rise in the numerical simulation in this study are plastic deformation heating and friction heating. Plastic deformation heating is estimated in the simulation as plastic work, W_p, as follows [17]:

$$W_p = \rho C \Delta T = \eta \int_{\varepsilon_p} \sigma_{eff} d\varepsilon_p \tag{1}$$

where, ρ is the density, C is the heat capacity, ΔT is the rate of temperature change, η is the energy conversion efficiency, ε_p is the plastic strain, and σ_{eff} is the effective stress. The energy density is determined by integrating the $\sigma_{eff} - \varepsilon_p$ curve. In this study, we set η=1. Friction heating was estimated as frictional work, W_f, as follows:

$$W_f = \rho C \Delta T = \int_S e_{fric} dS \tag{2}$$

where, S is the area of segment in contact surface and e_{fric} is the surface energy density which is the friction energy in contact surface [16].

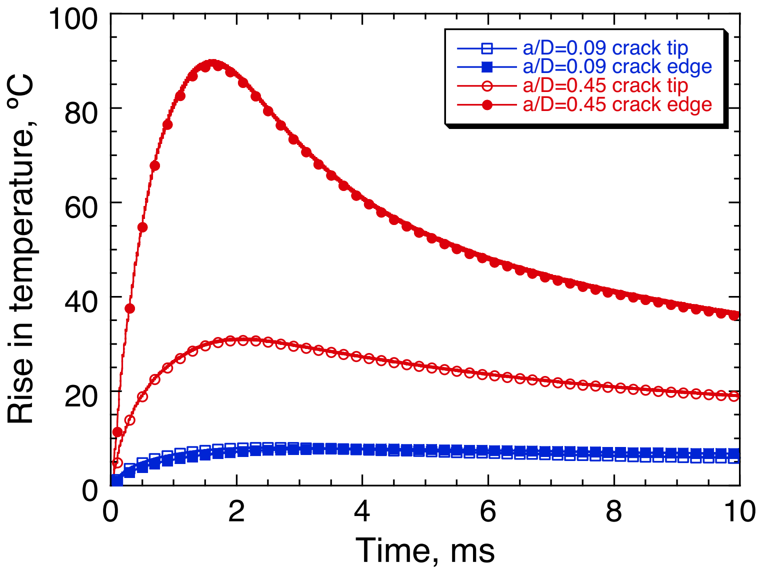

Fig. 13. Time histories of calculated rise in temperature at crack tip and crack edge for $a/D = 0.09$ and $a/D = 0.45$.

Fig. 13 shows the time histories of rise in temperature at the crack tip and edge for $a/D = 0.09$ and 0.45. For $a/D = 0.45$, the crack edge temperature increases rapidly and peaks at around 1.5 ms, the crack edge temperature is gradually increased and peaks at around 2 ms. Thereafter, both crack tip and crack edge temperatures are decrease gradually owing to heat conduction. By contrast, in the case of $a/D = 0.09$, both of crack edge and crack tip temperatures increased gradually until around 2 ms, and then, the temperatures remain constant owing to equilibrium between heating and the heat conduction.

Cross-sectional distributions of the specimen temperature, plastic strain correlated with the strain energy density, and surface energy density at the crack position for the crack lengths ratios of $a/D = 0.09$ and 0.45 obtained from the

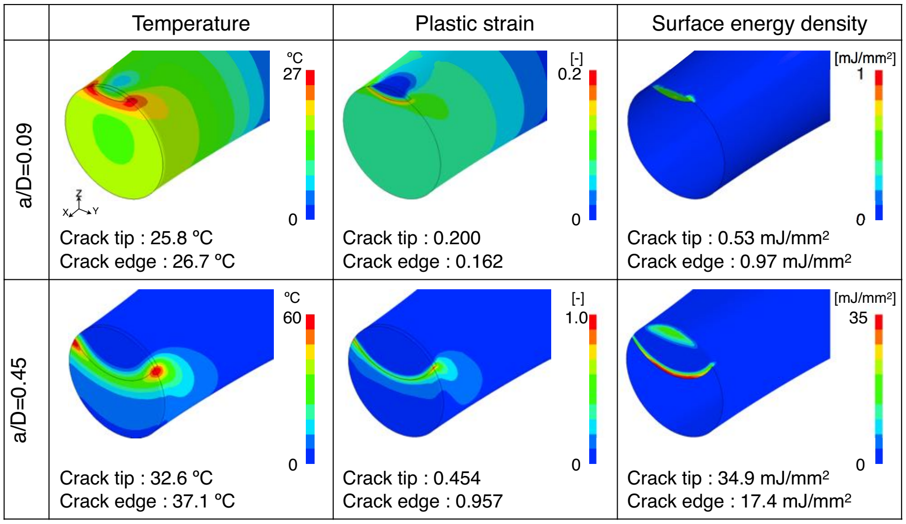

Fig. 14. Calculated temperature, plastic stain, and surface energy distributions for $a/D = 0.09$ and $a/D = 0.45$ at 10 ms.

simulations are shown in Fig. 14. The contours denote the distribution at 10 ms (the maximum calculation time) when the strain and friction energies peaks. It can be seen that the maximum temperature for $a/D = 0.45$ is higher than that for $a/D = 0.09$, and the maximum temperature was found at the crack edge, regardless of crack length. In the case of a/D=0.45, plastic strain at the crack edge is larger than that at the crack tip, and the distribution is well correlated with the temperature distribution. By contrast, surface energy density at the crack edge is lower than that at the crack tip. In the case of $a/D = 0.09$, in contrast, plastic strain at the crack tip is slightly larger than that at the crack edge, whereas the maximum temperature was found at the crack edge.

The maximum temperature rise of the crack edge and the crack tip for each crack length were estimated from the time responses and are shown in Fig. 15.

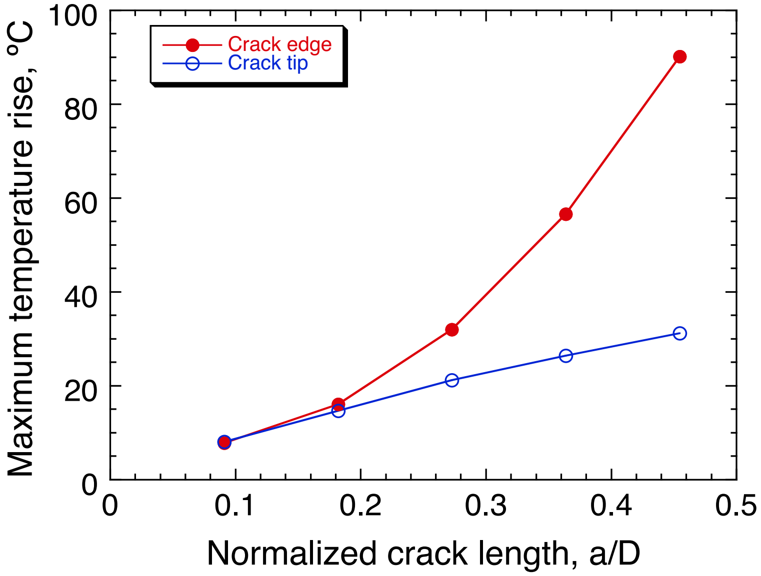

Fig. 15. Change in temperature rise as a function of normalized crack length.

The maximum temperature rise increase with increasing crack length, regardless of location. The rate of temperature increase as a function of crack length at the crack edge is larger than that at the crack tip.

Fig. 16 shows the change in plastic strain and surface energy density as a function of crack length, as obtained from the simulations. It can be seen that the change in plastic strains as a function of crack length is well correlated with the change in the maximum temperature, as shown in Fig. 15. By contrast, for a/D = 0.45, the surface energy density at the crack tip increases abruptly. This may be ascribed to the occurrence of beating around the crack tip due to the long crack. In all cases, surface energy density was of the order of tens of mJ/mm^2, whereas it was approximately higher than 100 mJ/mm^2 for the apparent temperature rise in the exploratory analysis which was conducted by forcedly sliding two plates using

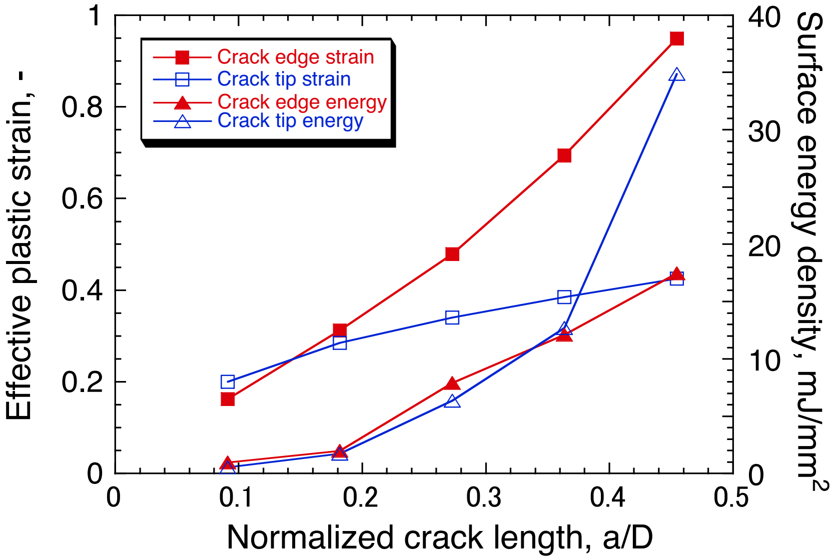

Fig. 16. Change in maximum plastic strain and maximum surface energy density as a function of normalized crack length.

the same material model as this study. Therefore, it is concluded that the apparent temperature rise just before failure was caused mainly by plastic deformation at the crack tip.

5. Conclusion

Evaluation of the gigacycle fatigue strength of 316L stainless steel, which is used as the structural material for the mercury target vessel, through an ultrasonic fatigue test as a fundamental study for detecting the initiation and propagation of fatigue crack by a remote and non-destructive measurement was performed. The following was concluded:

(1) An obvious fatigue limit was not observed below 10^9 cycles, regardless of

cold work.

(2) Abrupt temperature rise just before failure during the ultrasonic fatigue test was observed using thermography. It was confirmed that the peak temperature location existed on the crack tip and it moved with crack propagation. In future studies, we plan to increase temperature and time resolutions of the thermography instrument for improving the precision of detection of fatigue crack initiation.

(3) The mechanism of the temperature rise just before failure in ultrasonic fatigue test was investigated by performing a FE simulation focusing on plastic strain, friction, and beating of the fracture surface, and the result showed that plastic strain is the dominant factor underlying the abrupt temperature rise.

Acknowledgments

This work was partly supported by JSPS KAKENHI Grant Numbers JP26820016, JP17K14565. We would like to thank Mr. Kihei Tsutsui of Lancemore Co. for fruitful advising the FEM simulation by LS-DYNA.

[1] M. Futakawa, Targetry overview –various target concepts and expectable next generation targets in power frontier applications–, JPS Conf. Proc. 8 (2015) 001002–1–12.

[2] Neutron Source Section, Technical Design Report of Spallation Neutron Source Facility in J-PARC, Japan Atomic Energy Agency, 2012, JAEA-Technology, 2011-035.

[3] Y. Furuya, S. Motsuoka, T. Abe, K. Yamaguchi, Gigacycle fatigue properties for high-strength low-alloy steel at 100 Hz, 600 Hz, and 20 kHz, Scripta Mater. 46 (2002) 157–162.

[4] K. Takahashi, T. Ogawa, Evaluation of giga-cycle fatigue properties of austenitic stainless steels using ultrasonic fatigue test, J. Solid Mech. Mater. Eng. 2 (2008) 366–373.

[5] T. Ogawa, M. Nakane, K. Masaki, S. Hashimoto, Y. Ochi, K. Asano, Investigation of effect of pre-strain on very high-cycle fatigue strength of austenitic stainless steels, J. Power Energy Sys. 3 (2009) 38–50.

[6] D. A. McClintock, B. J. Vevera, B. W. Riemer, F. X. Gallmeier, J. W. Hyres, P. D. Ferguson, Post-irradiation tensile properties of the first and second operational target modules at the Spallation Neutron Source, J. Nucl. Mater. 450 (2014) 130–140.

[7] Z. Xiong, M. Futakawa, T. Naoe, K. Maekawa, Very high cycle fatigue in pulsed high power spallation neutron source, Adv. Mater. Res. 891–892 (2014) 536–541.

[8] T. Naoe, Z. Xiong, M. Futakawa, Gigacycle fatigue behavior of austenitic stainless steels used for mercury target vessel, J. Nucl. Mater. 468 (2016) 331–338.

[9] T. Sakagami, Y. Izumi, N. Mori, S. Kubo, Development of self-reference lock-in thermography and its application to remote nondestructive inspection of fatigue cracks in steel brides, Quant. Infrared Thermography J. 7 (2010) 73–84.

[10] M. P. Luong, Infrared thermographic scanning of fatigue in metals, Nucl. Eng. Des. 158 (1995) 363–376.

[11] A. Akai, D. S. T. Sakagami, Fatigue limit evaluation for austenitic stainless steel, J. Soc. Mater. Sci. 61 (2012) 953–959, In Japanese.

[12] D. Wagner, N. Ranc, C. Bathias, P. C. Paris, Fatigue crack initiation detection by an infrared thermography method, Fatigue Fract. Eng. Mater. Struct. 33 (2009) 12–21.

[13] D. Krewerth, A. Weinder, H. Biermann, Application of in situ thermography for evaluating the high-cycle and very high-cycle fatigue behavior of cast aluminium alloy AlSi7Mg(T6), Ultrasonics 53 (2013) 1441–1449.

[14] N. Ranc, D. Wagner, P. C. Paris, Study of thermal effects associated with crack propagation during very high cycle fatigue tests, Acta Mater. 56 (2008) 4012–4021.

[15] K. Salama, R. K. Lamerand, The prediction of fatigue life using ultrasound testing, in: Ultrasonic fatigue : proceedings of the First International Conference on Fatigue and Corrosion Fatigue Up to Ultrasonic Frequencies, Metallurgical Society of AIME, Pennsylvania, USA, 1982, pp. 109–118.

[16] Livermore Software Technology Corporation, LS-DYNA Theory Manual (2016).

[17] Çaldichoury, F. D. Pin, P. L'Eplattenier, D. Lorenz, N. Karajan, Coupling possibilities in LS-DYNA: Development status and sample applications, NAFEMS European Conference: Multiphysics Simulation 2012, 16–17 October 2012, Frankfurt, Germany (2012).